Available online at www.sciencedirect.com
ScienceDirect
Trans. Nonferrous Met. Soc. China 33(2023) 2365−2378
Transactions of Nonferrous Metals Society of China
www.tnmsc.cn

Effect of continuous multistep hydrogenation treatment step on microstructures and room-temperature compressive properties of TC21 alloy

Bao-guo YUAN[1], Ai-chuang TANG[1], De-guo QIAN[1], Qiang CHEN[2]

1. School of Materials Science and Engineering, Hefei University of Technology, Hefei 230009, China;
2. Southwest Technology and Engineering Research Institute, Chongqing 400039, China

Received 18 March 2022; accepted 19 May 2022

Abstract: The effect of continuous multistep hydrogenation treatment (CMHT) step on the microstructure of TC21 alloy was investigated by OM, XRD and TEM. Compressive properties of CMHT-processed TC21 alloys under diverse compressive velocities were also studied through room-temperature compression experiments. Results showed that the amount of α phase decreased and the amount of β phase and δ hydride increased as the CMHT step increased. α' martensite occurred only in TC21 alloy processed by one step CMHT. The deformation limit of CMHT-processed TC21 alloys showed the same change law under diverse compressive velocities, which decreased first, then increased, and finally decreased again as the CMHT step increased. The maximum increase of the deformation limit of TC21 alloy after CMHT reached 93.96% as compared to the original TC21 alloy. Reasons for the change of compressive properties of TC21 alloy processed by CMHT were analyzed.

Key words: TC21 alloy; continuous multistep hydrogenation treatment; microstructure; room-temperature compressive property

1 Introduction

Since the 21st century, the consumption of resources on the earth continues to increase, leading to the increasingly scarce resources and environmental deterioration. Numerous researchers are trying to find advanced structural materials with excellent performance to replace conventional materials [1−3]. The development directions of new products are lightweight, high reliability and long life. Titanium and titanium alloy materials have outstanding advantages [4−6], such as excellent corrosion resistance [7−9], high specific strength [10,11], good fatigue resistance and no magnetism [12−14]. Titanium industry develops rapidly due to the urgent needs of the aerospace technology [15]. The applications of titanium alloy in aerospace [16−18], shipbuilding [19−21], petrochemical [22−24], metallurgy and daily life are becoming wider and wider. TC21 alloy is a new type of α+β titanium alloy with high strength, high toughness and damage tolerance property [25], which is developed by the Northwest Institute for Nonferrous Metal Research (China) and has been applied in the fields of aerospace and civil [26−28]. Nonetheless, the room- temperature formability of TC21 alloy is poor due to its large deformation resistance and poor plasticity, limiting the further applications of TC21 alloy.

Fortunately, thermohydrogen treatment (THT), a type of technique to utilize hydrogen as a provisional alloying element in titanium alloy, can modify the microstructures and enhance the

Corresponding author: Qiang CHEN, Tel: +86-23-68792284, E-mail: 2009chenqiang@hfut.edu.cn, 2009chenqiang@163.com
DOI: 10.1016/S1003-6326(23)66265-X

mechanical properties of titanium alloy [29−31]. MA et al [32] studied the influence of hydrogen content on room-temperature compressive properties of Ti44Al6Nb alloy and found that the plasticity of Ti44Al6Nb alloy with 0.42 at.% H increased by 31% as compared to the original Ti44Al6Nb alloy. YUAN et al [33] researched the room-temperature compressive properties of TC21 alloy treated by THT at 750 °C and found that the deformation limit of TC21 alloy with 0.9 wt.% H increased by 30% as compared to the original TC21 alloy. In our previous work [34], we proposed a new type of THT, continuous multistep hydrogenation treatment (CMHT), to improve the compressive properties of Ti6Al4V alloy and found that the deformation limit of eight steps CMHT-processed Ti6Al4V alloy increased by 83.83% as compared to the original Ti6Al4V alloy. However, the effect of CMHT on the compressive properties of TC21 alloy was still not studied.

In this work, we studied the microstructures of TC21 alloy processed by CMHT at 850 °C under diverse CMHT steps. The effects of CMHT step and compressive velocity on the room-temperature compressive properties of TC21 alloy were also investigated. This work provided a new method to improve the room-temperature plasticity of TC21 alloy, which was beneficial to the room-temperature forming of TC21 alloy.

2 Experimental

Material employed in this work was TC21 alloy. Chemical composition of the as-received TC21 alloy was 7.69 Al, 2.09 Mo, 1.43 Cr, 1.74 Zr, 2.17 Sn, 1.72 Nb, and balance Ti (wt.%). TC21 alloy specimens with the size of *d*6 mm × 9 mm were first polished on a polishing machine, then washed in an ultrasonic cleaner, and finally dried. These operations ensured that the oxide layer on the specimen was removed and the surface of specimen was clean.

The process of CMHT was carried out in a tube-type furnace. Specimens were processed by CMHT at 850 °C under diverse CMHT steps (one step, four steps, seven steps, nine steps and eleven steps). The resistance furnace began to heat up with a velocity of 10 °C/min after the vacuum degree of the hydrogenation system was below 1.0×10^{-3} Pa. The tube-type furnace was first inflated with hydrogen of 11.325 kPa, and then inflated a certain quantity of hydrogen (10 kPa) at each interval of 1 h. After hydrogenation, the resistance furnace was pulled away from the location where the specimens were put, and then the specimens in the furnace tube were air cooled to room temperature. The change of hydrogen pressure in the process of CMHT was recorded by a digital manometer. The hydrogen pressure after holding for 1 h was recorded as equilibrium hydrogen pressure because the hydrogen absorption reaction was in an equilibrium stage at this moment. The hydrogen content of CMHT-processed specimen depended on the mass of the specimens before and after the process of CMHT. The mass of all specimens was measured using a high accuracy electronic balance with a sensitivity of 1×10^{-5} g. Hydrogen content in the CMHT-processed specimen was expressed as H/M (the ratio of hydrogen to metal atoms).

X-ray diffractometer (XRD, X'Pert PRO MPD, working voltage was 40 kV, working electricity was 40 mA, scanning velocity was 6 (°)/min) with Cu K_α radiation was used to investigate the phase composition of CMHT-processed specimens. The microstructural characterization was researched by optical microscopy (OM, YUESHI YM450R) and transmission electron microscopy (TEM, TECNAI G2 F20). OM specimens were ground and polished with sandpapers of 600#, 800# and 1000# grit serially, and the metallographic corrosion was carried out with etchant consisting of 1 mL HF, 2 mL HNO_3 and 6 mL H_2O. Foils for TEM research were polished to 100 μm and then milled through an ion milling facility (MODEL-691, working voltage was 5 kV, and incidence angle was 4°).

Room-temperature compression experiments were conducted with diverse compressive velocities (0.5, 5, 50, 100, 200 and 400 mm/min) on an axial/torsional test system (MTS landmark). The plastic degree was ruled as deformation limit ε_c, which was the strain value between ε_b (the ultimate compressive strain when the flow stress reached its maximum) and $\varepsilon_{0.2}$ (the 0.2% yield strain). The microhardness of specimens was measured using a digital microhardness tester (HVS−1000A) with a load of 4.9 N and a holding time of 30 s.

3 Results and discussion

3.1 Pressure−composition (P−C) isotherms

Figure 1(a) presents the P−C isotherms of TC21 alloy during the process of CMHT at 850 °C under diverse CMHT steps. The equilibrium hydrogen pressure during the process of CMHT increased nonlinearly as the H/M increased. The coincidence degree of these P-C isotherms was high, indicating that the results of CMHT experiments were credible. The difference between initial hydrogen pressure and equilibrium hydrogen pressure at each CMHT step was defined as ΔP, as shown in Fig. 1(b). ΔP decreased gradually as the CMHT step increased, illustrating that the reaction rate of hydrogen and titanium decelerated as the CMHT step increased when TC21 alloy was processed by CMHT at 850 °C.

3.2 OM observation

Figure 2 presents the optical microscopy images of the original TC21 alloy and alloys processed by CMHT at 850 °C under diverse CMHT steps. The original TC21 alloy consisted of a great number of white α phase and a few black β phase, as shown in Fig. 2(a). The microstructures of TC21 alloy changed apparently after being processed by CMHT at 850 °C under diverse CMHT steps. As shown in Fig. 2(b), when TC21 alloy was processed by one step CMHT, the contrast of α phase blackened and that of β phase whitened as compared to the original TC21 alloy. The electrochemical potential of β phase was enhanced when hydrogen was introduced into TC21 alloy at 850 °C, because hydrogen as a β stable element could enhance the electrochemical potential of β phase [35]. The electrochemical potential of α phase weakened due to the crystal defects and internal stresses caused by hydride in α phase [35]. A few fine α' martensite was discovered in TC21 alloy processed by one step CMHT, because some β phase transformed into α' martensite through the eutectoid reaction of $\beta \rightarrow \alpha'$ during the cooling stage of CMHT. Moreover, the amount of α phase decreased and the amount of β phase increased because hydrogen increased the stability of β phase [36]. Therefore, more β phase remained steady at room temperature. Microstructures of TC21 alloy were similar when the CMHT step was four, seven, nine and eleven, as shown in Figs. 2(c−f), respectively. The original α phase transformed into β phase and some bulbous α phase precipitated from β phase during the cooling stage of CMHT. β phase became the major phase due to the increase of hydrogen content, and clear β grain boundaries appeared in TC21 alloy when the CMHT step was four, seven, nine and eleven. As the CMHT step increased, β phase became more stabilized, because hydrogen content increased with increase of the CMHT step. The grain size was enlarged as the CMHT step increased because the holding time was longer at the higher CMHT steps.

3.3 XRD analysis

Figure 3 reveals the XRD patterns of the original TC21 alloy and alloys processed by CMHT at 850 °C under diverse CMHT steps. The original TC21 alloy contained a large amount of hexagonal close packed α phase and a small amount of body-

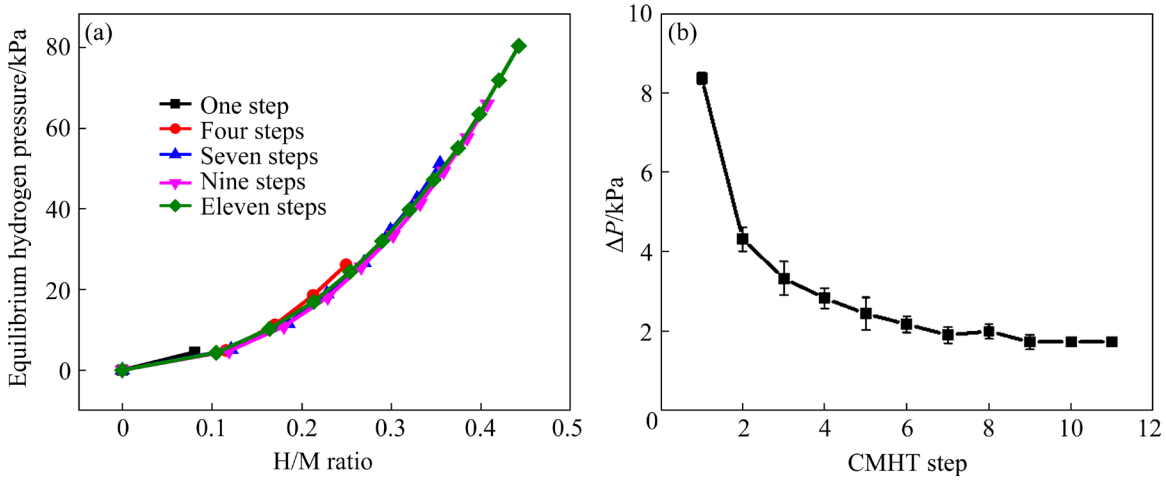

Fig. 1 P−C isotherms (a) and ΔP (b) of TC21 alloy during process of CMHT at 850 °C under diverse CMHT steps

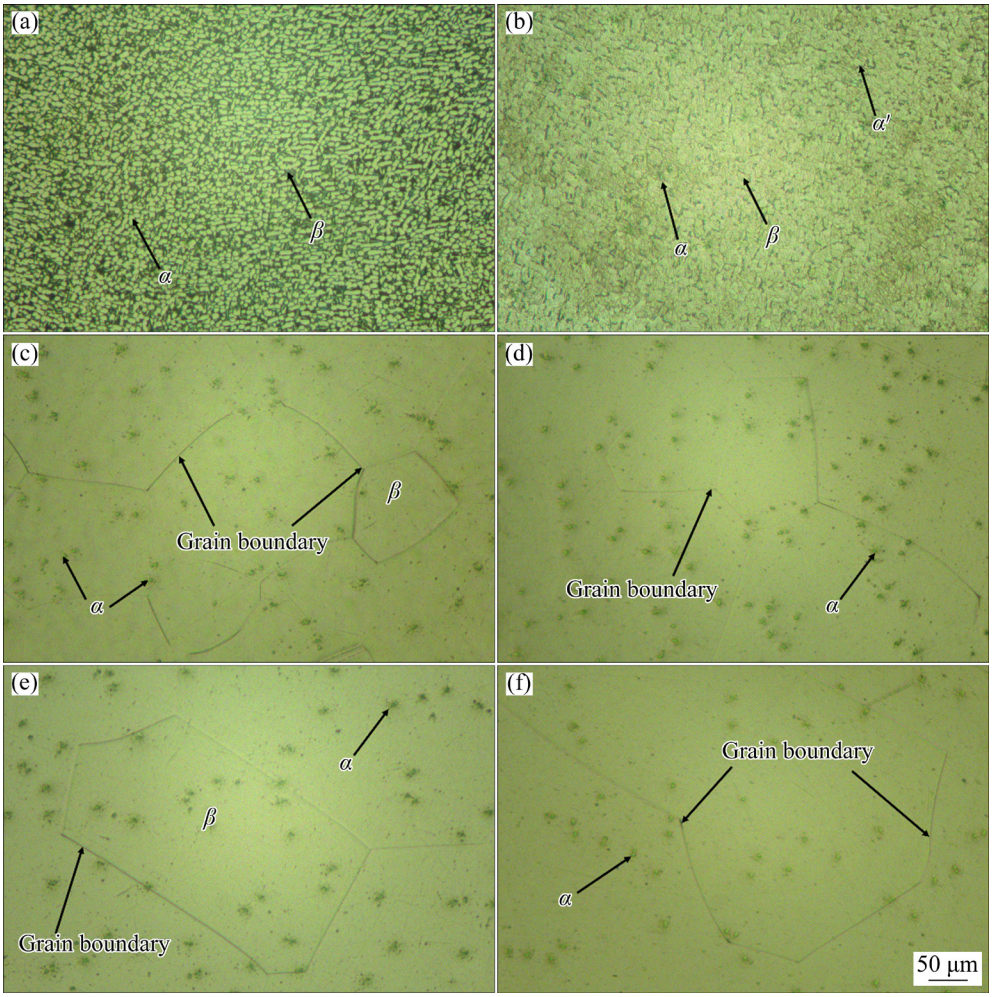

Fig. 2 Optical microscopy images of original TC21 alloy and alloys processed by CMHT at 850 °C under diverse CMHT steps: (a) Original; (b) One; (c) Four; (d) Seven; (e) Nine; (f) Eleven

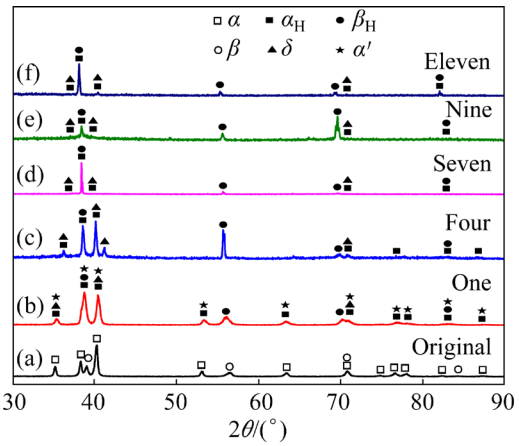

Fig. 3 XRD patterns of original TC21 alloy and alloys processed by CMHT at 850 °C under diverse CMHT steps

centered cubic β phase, as shown in Fig. 3(a). XRD patterns of TC21 alloy varied evidently after being processed by CMHT at 850 °C under diverse CMHT steps. As the CMHT step increased, the reflection peaks of α phase weakened or even vanished at some diffraction angles, indicating that the number of α phase decreased. The reflection peaks of β phase were enhanced, illustrating that the number of β phase increased. Because hydrogen as a β stable element was able to heighten the stability of β phase, more β phase was kept to room temperature due to the increase of hydrogen content in CMHT-processed TC21 alloys. The reflection peaks of δ hydride were observed in Figs. 3(b−f), which was also proved by the following TEM analysis. The lattice parameter of face-centered cubic δ hydride was calculated to be 0.444 nm [37].

3.4 TEM analysis

More meticulous microstructural information of the original TC21 alloy and alloys processed by CMHT at 850 °C under diverse CMHT steps was

characterized by TEM. The TEM micrographs of the original TC21 alloy are shown in Fig. 4. From Fig. 4(a), the original TC21 alloy consisted of platelet shape α phase and β phase, and the shape of β phase was restricted by α phase. The associated selected-area electron diffraction (SAED) patterns taken from α phase and β phase are shown in Fig. 4(a), the zone axes are $[\bar{1}101]_{\alpha}$ and $[\bar{1}11]_{\beta}$, respectively. High resolution transmission electron microscopy (HRTEM) analysis was employed to research the meticulous microstructural information of the original TC21 alloy and CMHT-processed TC21 alloys. Figures 4(b) and (c) show the HRTEM micrographs of α phase and β phase and the associated fast Fourier transformation (FFT) images of the zone marked. Figures 4(d) and (e) show the associated inverse FFT (IFFT) images of α phase zone marked in Fig. 4(b) and β phase zone marked in Fig. 4(c). The lattice image of α phase is indicated in Fig. 4(d) and the measured lattice interplanar distance of $(1\bar{1}02)_{\alpha}$ from the axis direction is 0.226 nm. The lattice image of β phase is indicated in Fig. 4(e) and the measured lattice interplanar distance of $(110)_{\beta}$ from the axis direction is 0.221 nm.

Figure 5 presents the TEM micrographs of TC21 alloy processed by one step CMHT at 850 °C. A number of α' martensite needles were detected in the alloy, some coarsened α phase lamellas were dispersed in the alloy. The associated SAED pattern taken from β phase and α' martensite is shown in Fig. 5(a), and the zone axes are $[1\bar{1}1]_{\beta}$ and $[11\bar{2}0]_{\alpha'}$, respectively. The orientation relationships between β phase and α' martensite are $(110)_{\beta}//(0001)_{\alpha'}$, $[1\bar{1}1]_{\beta}//[11\bar{2}0]_{\alpha'}$, which was consistent with the classical Burgers orientation relationship [38,39]. A small number of δ hydrides formed at α phase boundary, because there was high density of defect at phase boundary [40]. As shown in Figs. 5(b) and (c), the paralleled α' martensite needles distributed on the matrix. The associated SAED patterns taken from δ hydride and α' martensite are shown in Fig. 5(b), and the zone axes are $[01\bar{1}]_{\delta}$ and $[0001]_{\alpha'}$, respectively. Some fragmentary microstructures existed in the alloy, as shown in Fig. 5(c). Figure 5(d) presents the HRTEM micrograph of α' martensite and β phase, and the associated FFT images of α' martensite and β phase zone marked in

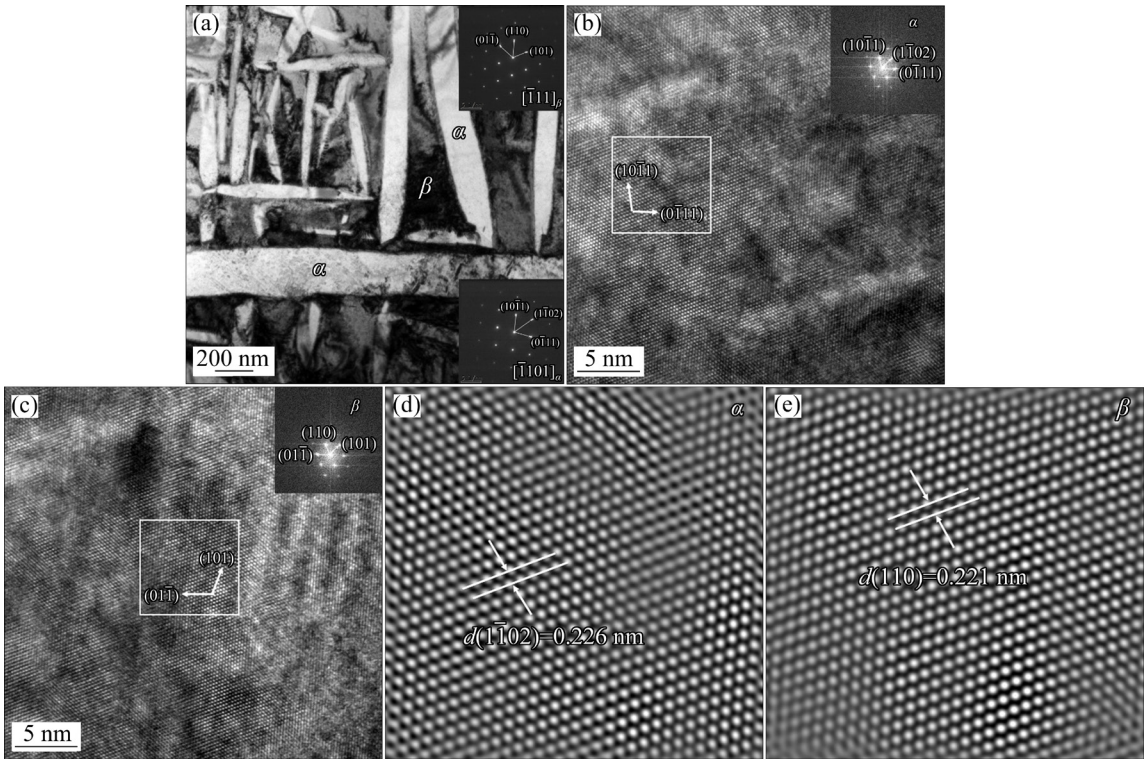

Fig. 4 TEM micrographs of original TC21 alloy: (a) Original α phase and β phase, and associated SAED patterns of α phase and β phase; (b) HRTEM micrograph showing α phase, and associated FFT image of α phase marked; (c) HRTEM micrograph showing β phase, and associated FFT image of β phase marked; (d) Associated IFFT image of α phase; (e) Associated IFFT image of β phase

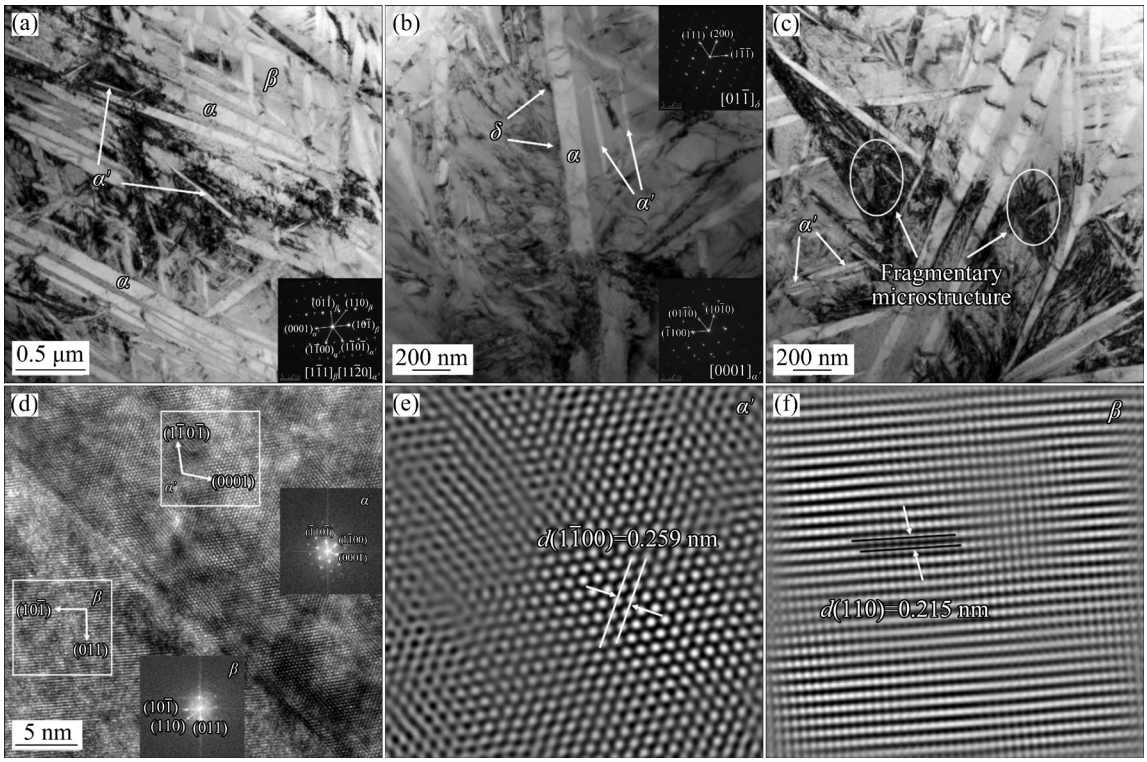

Fig. 5 TEM micrographs of TC21 alloy processed by one step CMHT at 850 °C: (a) α phase, α' martensite and β phase, and associated SAED pattern of α' martensite and β phase; (b) α phase, δ hydride and α' martensite, and associated SAED patterns of δ hydride and α' martensite; (c) α' martensite and fragmentary microstructure; (d) HRTEM micrograph showing β phase and α' martensite, and associated FFT images of β phase and α' martensite marked; (e) Associated IFFT image of α' martensite; (f) Associated IFFT image of β phase

the inset of Fig. 5(d). Figures 5(e) and (f) reveal the associated IFFT images of α' martensite and β phase zone marked in Fig. 5(d), respectively. The lattice image of α' martensite is indicated in Fig. 5(e) and the measured lattice interplanar distance of $(1\bar{1}00)_{\alpha'}$ from the axis direction is 0.259 nm. The lattice image of β phase is indicated in Fig. 5(f) and the measured lattice interplanar distance of $(110)_{\beta}$ from the axis direction is 0.215 nm.

Figure 6 shows the TEM micrographs of TC21 alloy processed by four steps CMHT at 850 °C. Some β phase lamellas were observed in the alloy when the CMHT step increased to four, indicating that the amount of β phase increased as compared to TC21 alloy processed by one step CMHT. Some δ hydrides formed at β phase boundary, and the associated SAED patterns taken from β phase and δ hydride are shown in Fig. 6(a), the zone axes are $[11\bar{1}]_{\beta}$ and $[10\bar{1}]_{\delta}$, respectively. When the CMHT step increased to four, α' martensite vanished as compared to TC21 alloy processed by one step CMHT. As shown in Figs. 6(b) and (c), some needle-like δ hydrides formed in the alloy, a number of fragmentary microstructures emerged in the alloy. Figure 6(d) reveals the HRTEM micrograph of δ hydride and the associated FFT image of the zone marked. Figure 6(e) shows the associated IFFT image of the zone marked in Fig. 6(d) and the lattice pattern of δ hydride. The measured lattice interplanar distance of $(1\,\bar{1}\,1)_{\delta}$ from the axis direction is 0.253 nm.

Figure 7 shows the TEM micrographs of TC21 alloy processed by seven steps CMHT at 850 °C. α phase lamellas distributed on the β phase matrix, as shown in Fig. 7(a). A few δ hydrides precipitated from α phase, indicating that the concentration of hydrogen in α phase exceeded the solubility of hydrogen in α phase. The associated SAED patterns taken from δ hydride and β phase are shown in Fig. 7(a), the zone axes are $[\bar{1}00]_{\delta}$ and $[1\,\bar{1}\,\bar{1}]_{\beta}$, respectively. Figure 7(b) shows a few paralleled α phase lamellas among the β phase matrixes, illustrating that the amount of β phase increased and the amount of α phase decreased as compared to the

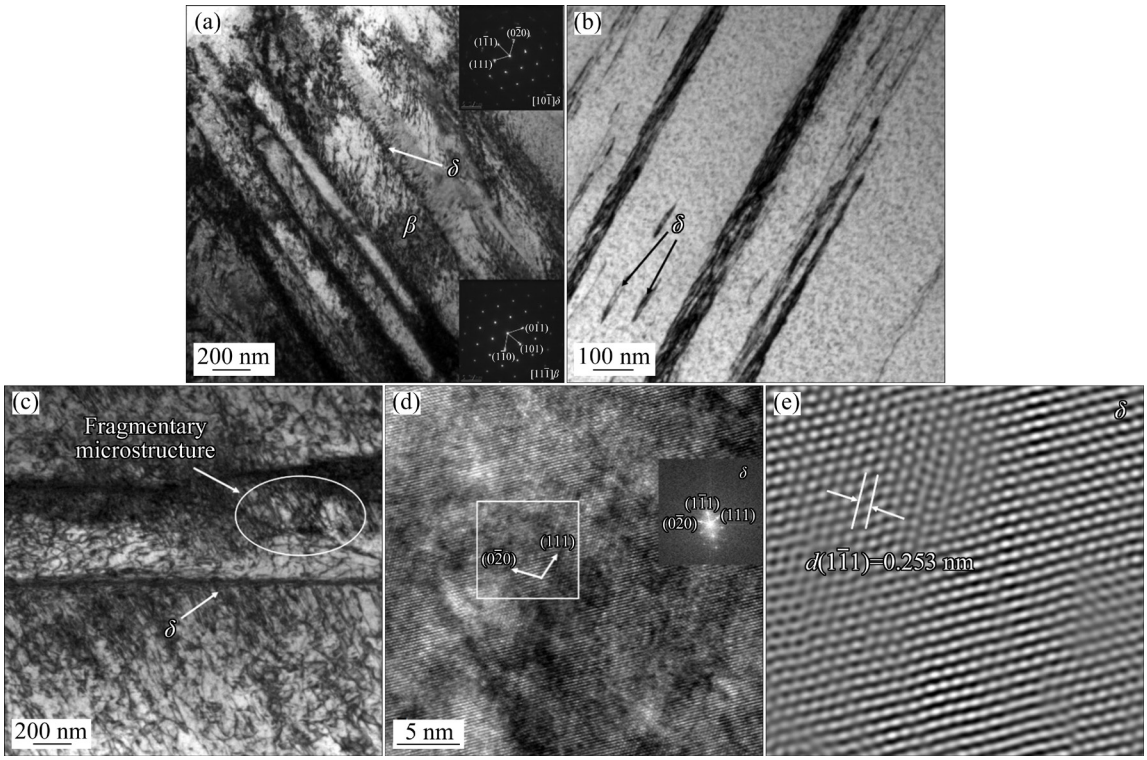

Fig. 6 TEM micrographs of TC21 alloy processed by four steps CMHT at 850 °C: (a) δ hydride and β phase, and associated SAED patterns of δ hydride and β phase; (b) δ hydride; (c) δ hydride and fragmentary microstructure; (d) HRTEM micrograph showing δ hydride, and associated FFT image of δ hydride marked; (e) Associated IFFT image of δ hydride

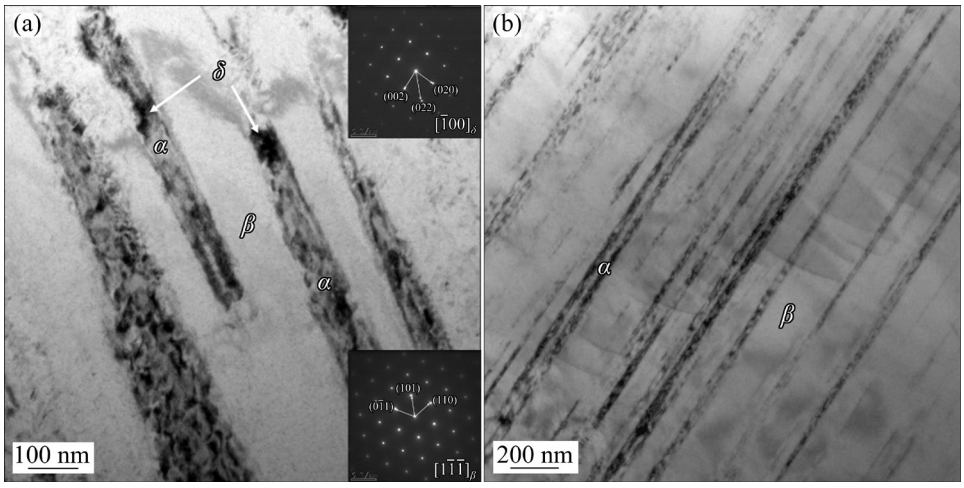

Fig. 7 TEM micrographs of TC21 alloy processed by seven steps CMHT at 850 °C: (a) δ hydride, α phase and β phase, and associated SAED patterns of δ hydride and β phase; (b) α phase and β phase

original TC21 alloy. Hydrogen as a β stable element could increase the stability of β phase. Therefore, more β phase was kept to room temperature when TC21 alloy was processed by seven steps CMHT.

Figure 8 shows the TEM micrographs of TC21 alloy processed by nine steps CMHT at 850 °C. As shown in Figs. 8(a) and (b), a number of δ hydrides occurred in TC21 alloy when CMHT step increased to nine, indicating that the number of δ hydride increased as compared to TC21 alloy processed by seven steps CMHT. The associated SAED patterns taken from δ hydride and β phase are shown in Fig. 8(a), the zone axes are $[001]_{\delta}$ and $[00\bar{1}]_{\beta}$, respectively. Figure 8(c) shows the HRTEM

micrograph of δ hydride and the associated FFT image of the zone marked. Figure 8(d) shows the associated IFFT image of the zone marked in Fig. 8(c) and the lattice pattern of δ hydride. The measured lattice interplanar distance of $(220)_{\delta}$ from the axis direction is 0.246 nm.

Figure 9 shows the TEM micrographs of TC21 alloy processed by eleven steps CMHT at 850 °C. Numerous β phase lamellas were observed in the alloy when the CMHT step increased further to eleven. As shown in Fig. 9(a), some δ hydrides precipitated directly from β phase, indicating that

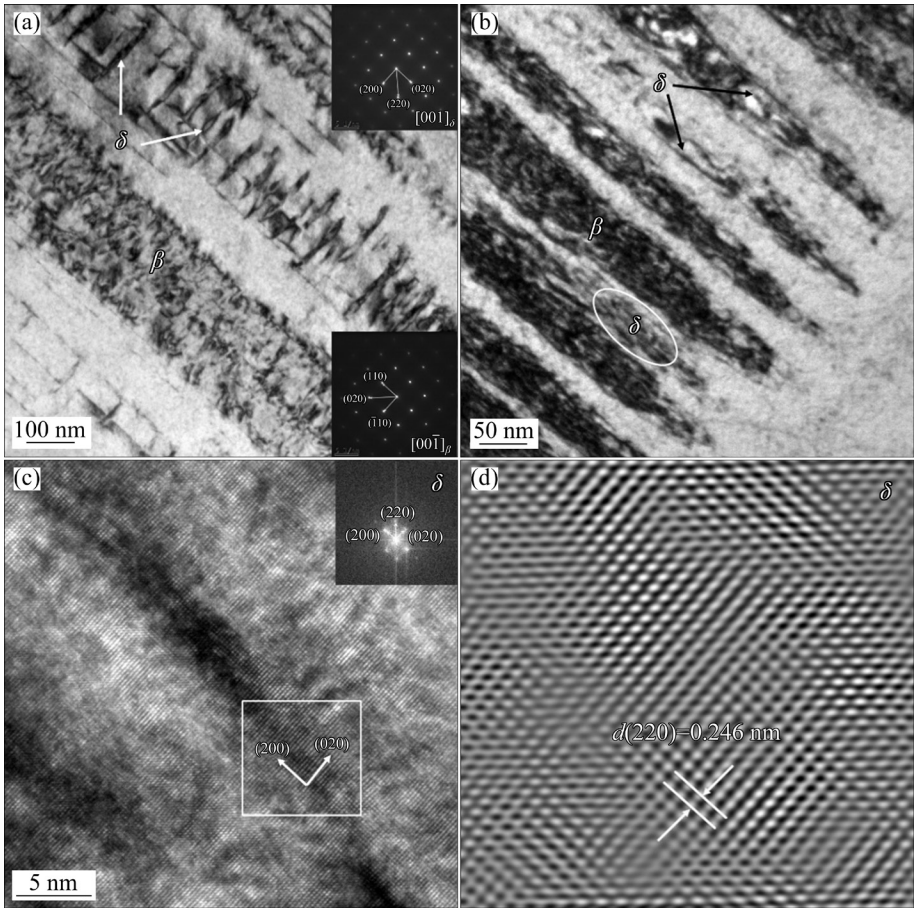

Fig. 8 TEM micrographs of TC21 alloy processed by nine steps CMHT at 850 °C: (a, b) δ hydride and β phase, and associated SAED patterns of δ hydride and β phase; (c) HRTEM micrograph showing δ hydride, and associated FFT image of δ hydride marked; (d) Associated IFFT image of δ hydride

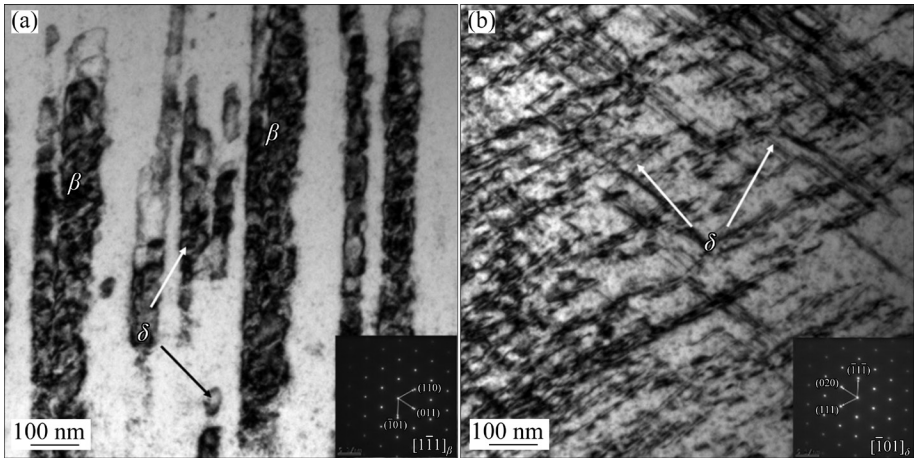

Fig. 9 TEM micrographs of TC21 alloy processed by eleven steps CMHT at 850 °C: (a) δ hydride and β phase, and associated SAED pattern of β phase; (b) δ hydride, and associated SAED pattern of δ hydride

the concentration of hydrogen in β phase exceeded the solubility of hydrogen in β phase. The associated SAED pattern taken from β phase is shown in Fig. 9(a), the zone axis is $[1\bar{1}1]_{\beta}$. A large amount of δ hydrides formed in the alloy, indicating that the amount of δ hydride increased as compared to TC21 alloy processed by nine steps CMHT. The associated SAED pattern taken from δ hydride is shown in Fig. 9(b), the zone axis is $[\bar{1}01]_{\delta}$.

3.5 Compressive properties

Figure 10 reveals the true stress−true strain curves of the original TC21 alloy and alloys processed by CMHT at 850 °C under diverse compressive velocities. The flow stress of TC21 alloy during the compression changed obviously after CMHT. The flow stress of one step CMHT-processed TC21 alloy was greater than those of the original TC21 alloy and other CMHT-processed

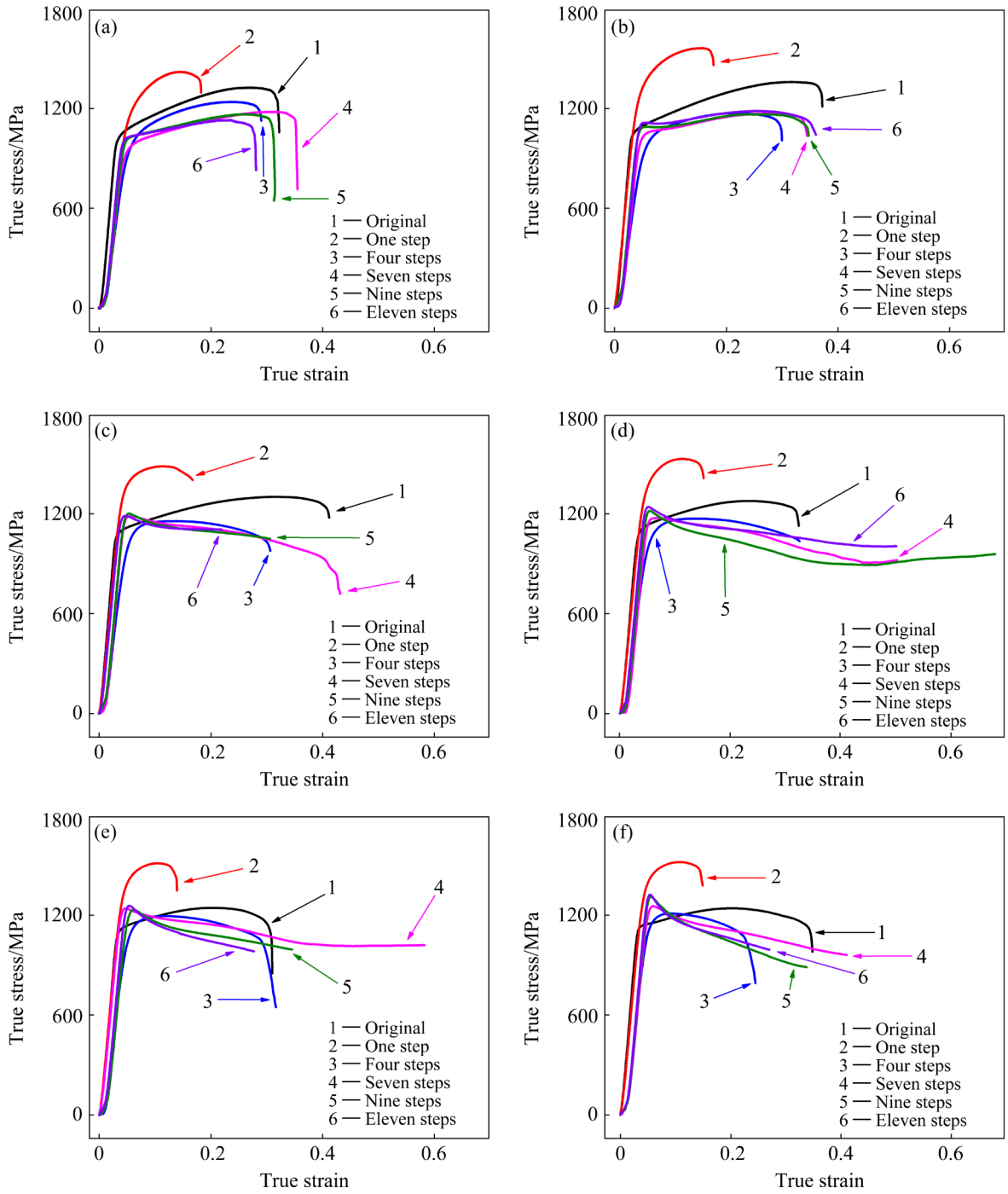

Fig. 10 True stress−true strain curves of original TC21 alloy and alloys processed by CMHT at 850 °C under diverse compressive velocities: (a) 0.5 mm/min; (b) 5 mm/min; (c) 50 mm/min; (d) 100 mm/min; (e) 200 mm/min; (f) 400 mm/min

TC21 alloys under each compressive velocity. However, the flow stresses of four, seven, nine and eleven steps CMHT-processed TC21 alloys were lower than that of the original TC21 alloy under each compressive velocity when true strain was in the range of 0.1−0.3. In addition, the change of flow stress with the increase of true strain was different for the original TC21 alloy and all CMHT-processed TC21 alloys under different compressive velocities. The flow stress increased with the increase of true strain, indicating that the work-hardening phenomenon was enhanced. The flow stress decreased with the increase of true strain, indicating that the softening phenomenon was enhanced. As shown in Fig. 10, when the compressive velocity was 0.5 mm/min, the work-hardening phenomenon was obvious for the original TC21 alloy and all CMHT-processed TC21 alloys. The work-hardening phenomenon weakened and the softening phenomenon was enhanced with the increase of compressive velocity for the original TC21 alloy and all CMHT-processed TC21 alloys. However, for the original TC21 alloy and one step CMHT-processed TC21 alloy, the work-hardening phenomenon was higher than the softening phenomenon under all compressive velocities. For the four, seven, nine and eleven steps CMHT-processed TC21 alloys, the work-hardening phenomenon was lower than the softening phenomenon under compressive velocities higher than 50 mm/min.

The deformation process included elastic deformation stage, yield stage, plastic deformation stage and fracture stage. There was no apparent yield stage from the true stress−true strain curves of the original TC21 alloy and CMHT-processed TC21 alloys. Therefore, the true stress to produce 0.20% true strain ($\sigma_{0.2}$) was taken as the yield strength of the alloy. Figure 11 reveals the yield strengths of the original TC21 alloy and alloys processed by CMHT at 850 °C under diverse compressive velocities. As the CMHT step increased, the yield strength of TC21 alloy showed the similar change law under diverse compressive velocities, which increased initially, then decreased, and finally increased again. When the compressive velocity was 0.5 mm/min, the yield strength of one step CMHT-processed TC21 alloy was greater than that of the original TC21 alloy. The yield strengths of four, seven, nine and eleven steps CMHT-processed TC21 alloys were lower than that of the original TC21 alloy. When the compressive velocity was 5 mm/min, the yield strengths of one, nine and eleven steps CMHT-processed TC21 alloys were greater than that of the original TC21 alloy. The yield strengths of four and seven steps CMHT-processed TC21 alloys were lower than that of the original TC21 alloy. When the compressive velocity was 50, 100, 200 and 400 mm/min, the yield strengths of one, seven, nine and eleven steps CMHT-processed TC21 alloys were greater than that of the original TC21 alloy. The yield strength of four steps CMHT-processed TC21 alloy was lower than that of the original TC21 alloy. The maximum decrease of the yield strength of TC21 alloy after CMHT reached 18.10% as compared to the original TC21 alloy (the CMHT step was four, and the compressive velocity was 200 mm/min). The maximum increase of the yield strength of TC21 alloy after CMHT reached 19.06% as compared to the original TC21 alloy (the CMHT step was eleven, and the compressive velocity was 400 mm/min).

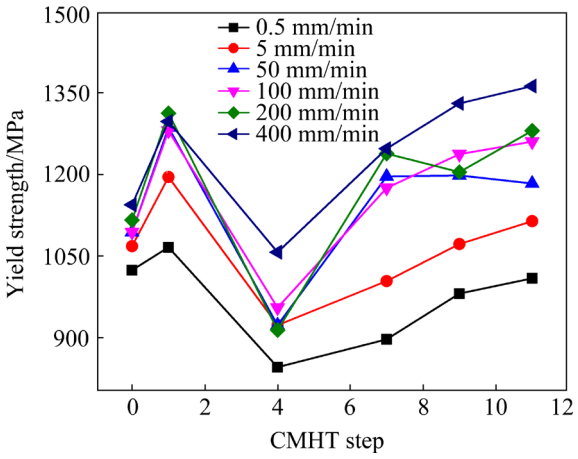

Fig. 11 Yield strengths of original TC21 alloy and alloys processed by CMHT at 850 °C under diverse compressive velocities

Figure 12 shows the deformation limits of the original TC21 alloy and alloys processed by CMHT at 850 °C under diverse compressive velocities. As the CMHT step increased, the deformation limits of CMHT-processed TC21 alloys showed the same change law under diverse compressive velocities, which decreased first, then increased, and finally decreased again. When the compressive velocity was 0.5 mm/min, the deformation limit of seven steps CMHT-processed TC21 alloy was greater than that of the original TC21 alloy. The deformation

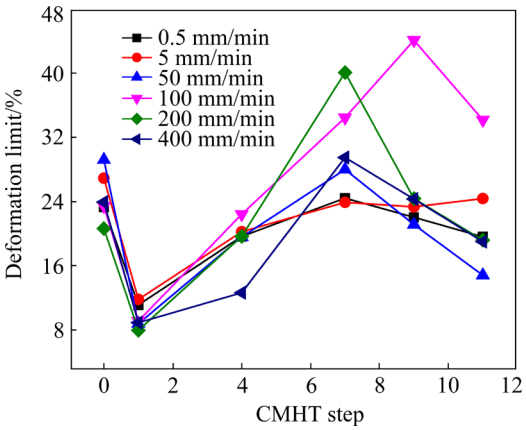

Fig. 12 Deformation limits of original TC21 alloy and alloys processed by CMHT at 850 °C under diverse compressive velocities

limits of one, four, nine and eleven steps CMHT-processed TC21 alloys were lower than that of the original TC21 alloy. When the compressive velocity was 5 and 50 mm/min, the deformation limits of all CMHT-processed TC21 alloys were lower than that of the original TC21 alloy. When the compressive velocity was 100 mm/min, the deformation limits of seven, nine and eleven steps CMHT-processed TC21 alloys were greater than that of the original TC21 alloy. The deformation limits of one and four steps CMHT-processed TC21 alloys were lower than that of the original TC21 alloy. When the compressive velocity was 200 and 400 mm/min, the deformation limits of seven and nine steps CMHT-processed TC21 alloys were greater than that of the original TC21 alloy. The deformation limits of one, four and eleven steps CMHT-processed TC21 alloys were lower than that of the original TC21 alloy. The maximum decrease of the deformation limit of TC21 alloy after CMHT reached 69.80% as compared to the original TC21 alloy (the CMHT step was one, and the compressive velocity was 50 mm/min). The maximum increase of the deformation limit of TC21 alloy after CMHT reached 93.96% as compared to the original TC21 alloy (the CMHT step was seven, and the compressive velocity was 200 mm/min).

Figure 13 reveals the microhardnesses of the original TC21 alloy and alloys processed by CMHT at 850 °C under diverse CMHT steps. The microhardness of TC21 alloy increased first, then decreased, and finally increased again as the CMHT step increased. The microhardness of one step CMHT-processed TC21 alloy was the maximum among those of all CMHT-processed TC21 alloys, which increased by 26.72% as compared to the original TC21 alloy. The microhardness of four steps CMHT-processed TC21 alloy was the minimum among those of all CMHT-processed TC21 alloys, which decreased by 34.99% as compared to the one step CMHT-processed TC21 alloy. When the CMHT step was greater than four, the microhardness increased gradually as the CMHT step increased.

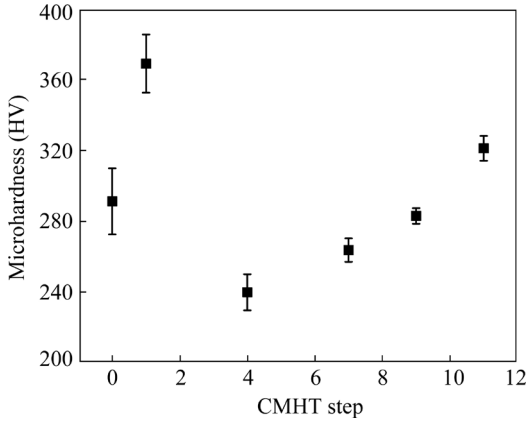

Fig. 13 Microhardnesses of original TC21 alloy and alloys processed by CMHT at 850 °C under diverse CMHT steps

3.6 Discussion

Based on the above results of microstructures and compressive properties, the microstructures and compressive properties of TC21 alloy changed obviously after being processed by CMHT at 850 °C under diverse CMHT steps. When the CMHT step was one, α' martensite occurred only in the alloy. Although both α phase and α' martensite had hexagonal close packed crystal structure, α' martensite was the supersaturated solid solution of α phase. Thus, the deformation limit of one step CMHT-processed TC21 alloy decreased as compared to the original TC21 alloy. The flow stress, yield strength and microhardness of one step CMHT-processed TC21 alloy increased as compared to the original TC21 alloy. When the CMHT step increased to four, α' martensite disappeared and β phase became the major phase in the alloy. Therefore, the four steps CMHT-processed TC21 alloy had higher deformation limit and lower flow stress, yield strength and microhardness as compared to the one step CMHT-processed TC21 alloy. When the CMHT step was

greater than four, the deformation limit of CMHT-processed TC21 alloys increased first and then decreased as the CMHT step increased. The increase of deformation limit of CMHT-processed TC21 alloys was related to the increase of the amount of β phase. The decrease of deformation limit of CMHT-processed TC21 alloys was caused by the increase of the amount of δ hydride. The increase of the amount of δ hydride also led to the increase of yield strength and microhardness of CMHT-processed TC21 alloys as the CMHT step increased. According to the above analysis, the compressive properties of TC21 alloy were mainly affected by microstructure evolution after CMHT.

With the increase of compressive velocity, the work-hardening phenomenon weakened and the softening phenomenon was enhanced during the process of compression for the original TC21 alloy and all CMHT-processed TC21 alloys. The work-hardening phenomenon was mainly caused by the accumulation and entanglement of dislocation [41]. The softening phenomenon was affected by the thermal energy generated by the plastic deformation [42]. When the compressive velocity increased, the dissipation of thermal energy was less during the compression, leading to the enhancement of softening phenomenon. Moreover, β phase became the major phase when the CMHT step was greater than one. Thus, the softening phenomenon was more obvious when the CMHT step was greater than one [43].

CMHT can improve the room-temperature deformation limit of TC21 alloy. It is more conducive to room-temperature plastic deformation for TC21 alloy if its deformation limit is higher. In this work, the maximum increase of the deformation limit of CMHT-processed TC21 alloys reached 93.96% as compared to the original TC21 alloy. The CMHT step and compressive velocity conducive to room-temperature plastic deformation for TC21 alloy are seven and 200 mm/min, or nine and 100 mm/min, respectively. After room-temperature plastic deformation, CMHT-processed TC21 alloys should be treated by vacuum annealing to remove hydrogen in order to avoid embrittlement in the period of service [44,45].

4 Conclusions

(1) As the CMHT step increased, the amount of α phase decreased and the amount of β phase and δ hydride increased. α' martensite occurred only in TC21 alloy processed by one step CMHT.

(2) The work-hardening phenomenon weakened and the softening phenomenon was enhanced with the increase of compressive velocity for the original TC21 alloy and all CMHT-processed TC21 alloys. For the original TC21 alloy and one step CMHT-processed TC21 alloy, the work-hardening phenomenon was higher than the softening phenomenon under all compressive velocities. For the four, seven, nine and eleven steps CMHT-processed TC21 alloys, the work-hardening phenomenon was lower than the softening phenomenon under compressive velocities higher than 50 mm/min.

(3) The yield strength of CMHT-processed TC21 alloys showed the similar change law under diverse compressive velocities, which increased initially, then decreased, and finally increased again as the CMHT step increased. The maximum decrease of the yield strength of TC21 alloy after CMHT reached 18.10% as compared to the original TC21 alloy. The deformation limit of CMHT-processed TC21 alloys showed the same change law under diverse compressive velocities, which decreased first, then increased, and finally decreased again as the CMHT step increased. The maximum increase of the deformation limit of TC21 alloy after CMHT reached 93.96% as compared to the original TC21 alloy.

Acknowledgment

This work was financially supported by the National Natural Science Foundation of China (No. 51875157).

References

[1] DU Hui, CAI Jia-hong, WANG Ya-song, YAO Jun-qing, CHEN Qiang, CUI Yu, LIU Xin-wang. Effect of partial recrystallization on microstructure and tensile properties of NiFeCoCrMn high-entropy alloy [J]. Transactions of Nonferrous Metals Society of China, 2022, 32: 947−956.

[2] WANG Ye, LI Feng, BIAN Nan, DU Hua-qiu, HUO Peng-da. Mechanism of plasticity enhancement of AZ31B magnesium alloy sheet by accumulative alternating back extrusion [J]. Journal of Magnesium and Alloys, 2023, 11(5): 1791−1801.

[3] CHEN Gang, WAN Jia, HE Ning, ZHANG Hong-ming, HAN Fei, ZHANG Yu-min. Strengthening mechanisms based on reinforcement distribution uniformity for particle reinforced aluminum matrix composites [J]. Transactions of Nonferrous Metals Society of China, 2018, 28: 2395−2400.

[4] XU Wei-feng, MA Jun, LUO Yu-xuan, FANG Yue-xiao. Microstructure and high-temperature mechanical properties of laser beam welded TC4/TA15 dissimilar titanium alloy joints [J]. Transactions of Nonferrous Metals Society of China, 2020, 30: 160−170.

[5] PENG He-li, LI Xi-feng, CHEN Xu, JIANG Jun, LUO Jing-feng, XIONG Wei, CHEN Jun. Effect of grain size on high-temperature stress relaxation behavior of fine-grained TC4 titanium alloy [J]. Transactions of Nonferrous Metals Society of China, 2020, 30: 668−677.

[6] FAN Rong-lei, WU Yong, CHEN Ming-he, XIE Lan-sheng. Relationship among microstructure, mechanical properties and texture of TA32 titanium alloy sheets during hot tensile deformation [J]. Transactions of Nonferrous Metals Society of China, 2020, 30: 928−943.

[7] YUAN Bao-guo, ZHANG Xiao-xue, WANG Yu-jie, CHEN Qiang, WAN Yuan-yuan, ZHENG Yu-bin, XING Zhi-hui, ZHAN Hong. Effects of cyclic thermo-hydrogen processing on microstructural and mechanical properties of Ti6Al4V alloy at room temperature [J]. Vacuum, 2020, 171: 109015.

[8] ZHAO Er-tuan, SUN Shi-chen, YU Jin-rui, AN Yu-kun, CHEN Wen-zhen, CHEN Rui-rui. Dynamic recrystallization and silicide precipitation behavior of titanium matrix composites under different strains [J]. Transactions of Nonferrous Metals Society of China, 2021, 31: 3416−3427.

[9] LIN Yong-cheng, TANG Yi, JIANG Yu-qiang, CHEN Jian, WANG Dan, HE Dao-guang. Precipitation of secondary phase and phase transformation behavior of a solution-treated Ti−6Al−4V alloy during high-temperature aging [J]. Advanced Engineering Materials, 2020, 22: 1901436.

[10] YANG Jian-hui, WEI Shi, WEI Ji, CHANG Ruo-han, LU Zi-chuan, XIAO Shu-long, CHEN Yu-yong, ZHOU Hai-tao. Microstructure evolution, mechanical properties and high temperature deformation of (TiB + TiC)/Ti−3.5Al−5Mo−6V−3Cr−2Sn−0.5Fe titanium alloy [J]. Materials Characterization, 2022, 184: 111616.

[11] CUI Shu-wan, SHI Yong-hua, ZHANG Cheng-shi. Microstructure and mechanical properties of TC4 titanium alloy K-TIG welded joints [J]. Transactions of Nonferrous Metals Society of China, 2021, 31: 416−425.

[12] CAO Xin, HE Wei-feng, LIAO Bin, HE Guang-yu, JIAO Yang, HUANG Da, WANG Shi-guang. Effect of TiN/Ti coating combined with laser shock peening pre-treatment on the fatigue strength of Ti−6Al−4V titanium alloy [J]. Surface and Coatings Technology, 2020, 403: 126393.

[13] XU Xu, XUE Qi-wen, HE Yi-qian. Nonlinear fatigue life prediction model based on material memory [J]. Journal of Mechanical Science and Technology, 2020, 34: 5029−5039.

[14] XU Jian-wei, ZENG Wei-dong, ZHOU Da-di, HE Sheng-tong, JIA Run-chen. Evolution of coordination between α and β phases phases for two-phase titanium alloy during hot working [J]. Transactions of Nonferrous Metals Society of China, 2021, 31: 3428−3438.

[15] DENG Yun-hua, GUAN Qiao, TAO Jun. Effect of heating time on bonding interface, atom diffusion and mechanical properties of dissimilar titanium joints produced by thermal self-compressing bonding [J]. Transactions of Nonferrous Metals Society of China, 2018, 28: 662−668.

[16] HUA Ke, ZHANG Yong-liang, ZHANG Fan, KOU Hong-chao, LI Xiao-lin, WU Hong-xing, WANG Hai-feng. Microstructure refinement and enhanced wear-resistance modulated by stress relaxation processing in a metastable beta titanium alloy [J]. Materials Characterization, 2021, 181: 111505.

[17] HU Y T, LI S C, YU Q, CHEN Z Y, VADIM S. Investigation of tensile and compressive mechanical properties of typical aerospace alloy materials [J]. Transactions of the Canadian Society for Mechanical Engineering, 2021, 45: 612−625.

[18] XIE Gui-bai, BAI Hong-wu, MIAO Guang-hui, FENG Guo-bao, YANG Jing, HE Yun, LI Xiao-jun, LI Yun. The applications of ultra-thin nanofilm for aerospace advanced manufacturing technology [J]. Nanomaterials, 2021, 11: 3282.

[19] SUN Cheng-qi, LI Yan-qing, XU Kui-long, XU Bao-tong. Effects of intermittent loading time and stress ratio on dwell fatigue behavior of titanium alloy Ti−6Al−4V ELI used in deep-sea submersibles [J]. Journal of Materials Science and Technology, 2021, 77: 223−236.

[20] CHEN Quan, ZHANG Jia-jia, HUANG An-guo, WEI Peng-yu. Study on wear resistance of Ti−6Al−4V alloy composite coating prepared by laser alloying [J]. Applied Sciences, 2021, 11: 446.

[21] NI Rui-yang, HOU Wen-tao, SHEN Yi-fu, LIU Wen-ming, CAO Fu-jun, SUN Tao. Friction forge riveting: A new joining method for connecting 40Cr steel and TC4 titanium alloy [J]. Journal of Manufacturing Processes, 2021, 68: 79−89.

[22] LUO J, DONG H, BELL T. Model-based contact fatigue design of surface engineered titanium gears [J]. Computational Materials Science, 2006, 35: 447−457.

[23] HE Qian-feng, SI Shi-hui, SONG Le-shan, YAN Hai-yan, YAO Yong-ge, ZHAO Di, CAI Qun-huan. Refractory petrochemical wastewater treatment by $K_2S_2O_8$ assisted photocatalysis [J]. Saudi Journal of Biological Sciences, 2019, 26: 849−853.

[24] LI X, WANG G Y, HU Y W, IRADUKUNDA Y, LUO F F, YI K Q, SHI G F. Sulfonated carbon-titanium dioxide composite nanofiber tube catalysts for dehydration of sugars in biphasic solvents to obtain 5-hydroxymethylfurfural [J]. Journal of the Taiwan Institute of Chemical Engineers, 2021, 129: 26−39.

[25] ELSHAER R N, IBRAHIM K M. Effect of cold deformation and heat treatment on microstructure and mechanical properties of TC21 Ti alloy [J]. Transactions of Nonferrous Metals Society of China, 2020, 30: 1290−1299.

[26] WANG Ke, WU Ming-yu, REN Zhao, ZHANG Yu, XIN Ren-long, LIU Qing. Static globularization and grain morphology evolution of alpha and beta phases during annealing of hot-rolled TC21 titanium alloy [J]. Transactions of Nonferrous Metals Society of China, 2021, 31: 2664−2676.

[27] YUAN Bao-guo, CHEN Wen-jie, TANG Ai-chuang, QIAN De-guo, SONG Yang-xi, CHEN Qiang, ZHANG Xiao-xue. Non-isothermal phase transformation behavior and thermal expansion characteristics of TC21 alloy [J]. Journal of Materials Engineering and Performance, 2021, 30: 7926−7934.

[28] SHI Zhi-feng, GUO Hong-zhen, ZHANG Jian-wei, YIN Jian-ning. Microstructure-fracture toughness relationships and toughening mechanism of TC21 titanium alloy with lamellar microstructure [J]. Transactions of Nonferrous Metals Society of China, 2018, 28: 2440−2448.

[29] SUN Zhong-gang, HOU Hong-liang, ZHOU Wen-long, WANG Yao-qi, LI Zhi-qiang. The effect of hydrogen on microstructures evolution and deformation behaviors of Ti−6Al−4V alloys [J]. Journal of Alloys and Compounds, 2009, 476: 550−555.

[30] YUAN Bao-guo, YU Hai-ping, LI Chun-feng. Influence of

hydrogen content on room temperature compressive properties of Ti−6Al−4V alloy at high strain rate [J]. Transactions of Nonferrous Metals Society of China, 2012, 22: 2943−2951.
[31] REN Ya-fei, ZHAO Jun, XIE Hua-sheng, LIU Shi-bing, LUO Yan-chun, YAN Ping. Influence of thermo hydrogen treatment on microstructure and mechanical properties of Ti−5Al−2.5Sn ELI alloy [J]. China Foundry, 2017, 14: 55−58.
[32] MA T F, CHEN R R, ZHENG D S, GUO J J, DING H S, SU Y Q, FU H Z. Hydrogen enhanced the room-temperature compressive properties of Ti44Al6Nb alloy [J]. Materials Letters, 2018, 213: 170−173.
[33] YUAN Bao-guo, ZHENG Yu-bin, GONG Long-qing, CHEN Qiang, LV Meng. Effect of hydrogen content on microstructures and room-temperature compressive properties of TC21 alloy [J]. Materials and Design, 2016, 94: 330−337.
[34] YUAN Bao-guo, DU Jiang-fei, ZHANG Xiao-xue, CHEN Qiang, WAN Yuan-yuan, XING Zhi-hui, ZHAN Hong. Microstructures and room-temperature compressive properties of Ti6Al4V alloy processed by continuous multistep hydrogenation treatment [J]. International Journal of Hydrogen Energy, 2020, 45: 25567−25579.
[35] WANG Xiao-li, ZHAO Yong-qing, WEI Xiao-wei, HOU Hong-liang. Microstructures of TC21 alloys after hydrogenation and dehydrogenation [J]. Transactions of Nonferrous Metals Society of China, 2014, 24: 82−88.
[36] NATALIA P, ALEXEY P, MAXIM S, EGOR K, VIKTOR K, OLGA P, ROMAN L, ANDREY L, ANDREY K. Hydrogen-induced phase transformation and microstructure evolution for Ti−6Al−4V parts produced by electron beam melting [J]. Metals, 2018, 8: 301.
[37] YUAN Bao-guo, LIU Xing, DU Jiang-fei, CHEN Qiang, WAN Yuan-yuan, XIANG Yun-liang, TANG Yan, ZHANG Xiao-xue, HUANG Zhong-yue. Effects of hydrogenation temperature on room-temperature compressive properties of CMHT-treated Ti6Al4V alloy [J]. Journal of Materials Science and Technology, 2021, 72: 132−143.
[38] WANG Duo-duo, FUN Qun-bo, YANG Lin, GONG Hai-chao, YUAN Jing-jiu, CHEN Kai, ZHU Xin-jie, CHENG Xing-wang, ZHOU Zhi-ming. Effects of rolling reduction on Burgers orientation relationship and slip behavior of a Ti−5.5Mo−7.2Al−4.5Zr−2.6Sn−2.1Cr alloy [J]. Journal of Materials Research and Technology, 2021, 15: 3099−3109.
[39] GAO Xiong-xiong, ZHANG Sai-fei, WANG Lei, YANG Kun, WANG Peng, CHEN Hong-yuan. Evolution of grain boundary α phase during cooling from β phase field in a $\alpha+\beta$ titanium alloy [J]. Materials Letters, 2021, 301: 130318.
[40] WANG Xue-li, LI Fu-guo, XU Tian-yu, MA Xin-kai, HOU Bo-tong, LUO Liang, LIU Bang. Microstructure and microhardness evolution of Ti−10V−2Fe−3Al alloy under tensile/torsional deformation modes [J]. Journal of Alloys and Compounds, 2021, 881: 160484.
[41] CAI M H, LEE C Y, LEE Y K. Effect of grain size on tensile properties of fine-grained metastable β titanium alloys fabricated by stress-induced martensite and its reverse transformations [J]. Scripta Materialia, 2012, 66: 606−609.
[42] SU Nan, CHEN Ming-he, XIE Lan-sheng, LOU Feng, SHI Wen-xiang. Dynamic mechanical characteristics and constitutive model of TC2 Ti-alloy [J]. Chinese Journal of Materials Research, 2021, 35: 201−208. (in Chinese)
[43] HUA Ke, WAN Qiong, KOU Hong-chao, ZHANG Fan, ZHANG Yong-liang, LI Jin-shan. The interplay relationship between phase transformation and deformation behavior during hot compression in a metastable β titanium alloy [J]. Materials & Design, 2021, 197: 109275.
[44] ZHANG Xiao-xue, ZHENG Yu-bin, YUAN Bao-guo. Dehydrogenation technology of hydrogenated TC21 alloy [J]. Journal of Alloys and Compounds, 2017, 695: 1444−1447.
[45] JIA Yun-ping, HU Shuang-lin, ZHOU Xiao-song, PENG Shu-ming. Interactions between hydrogen and the $(11\bar{2}1)$ twin boundary in hexagonal close-packed titanium [J]. International Journal of Hydrogen Energy, 2020, 45: 9854−9864.

连续多步置氢处理步数对 TC21 合金显微组织和室温压缩性能的影响

袁宝国[1]，汤爱闯[1]，钱德国[1]，陈 强[2]

1. 合肥工业大学 材料科学与工程学院，合肥 230009；
2. 西南技术工程研究所，重庆 400039

摘 要：采用 OM、XRD 和 TEM 方法研究连续多步置氢处理步数对 TC21 合金显微组织的影响。通过室温压缩实验研究连续多步置氢 TC21 合金在不同压缩速度下的压缩性能。结果表明：随着连续多步置氢处理步数的增加，α 相的含量减少，β 相和 δ 氢化物的含量增多，仅置氢 1 步时 TC21 合金中出现 α'马氏体。连续多步置氢 TC21 合金的极限变形率在不同压缩速度下的变化规律相同，即随着连续多步置氢处理步数的增加，极限变形率先减小再增大最后又减小。连续多步置氢处理后，TC21 合金的极限变形率比原始 TC21 合金最大增幅达到 93.96%。分析了连续多步置氢 TC21 合金压缩性能变化的原因。

关键词：TC21 合金；连续多步置氢处理；显微组织；室温压缩性能

(Edited by Xiang-qun LI)